Science Advances
AAAS

Supplementary Materials for

Respiratory delivery of single low-dose nebulized PFCE-C25 NEs for lymphatic transport and durable stimulation of antitumor immunity in lung cancer

Rong A *et al.*

Corresponding author: Xilin Sun, sunxl@ems.hrbmu.edu.cn

Sci. Adv. **10**, eadp7561 (2024)
DOI: 10.1126/sciadv.adp7561

This PDF file includes:

Figs. S1 to S27

Supplementary information

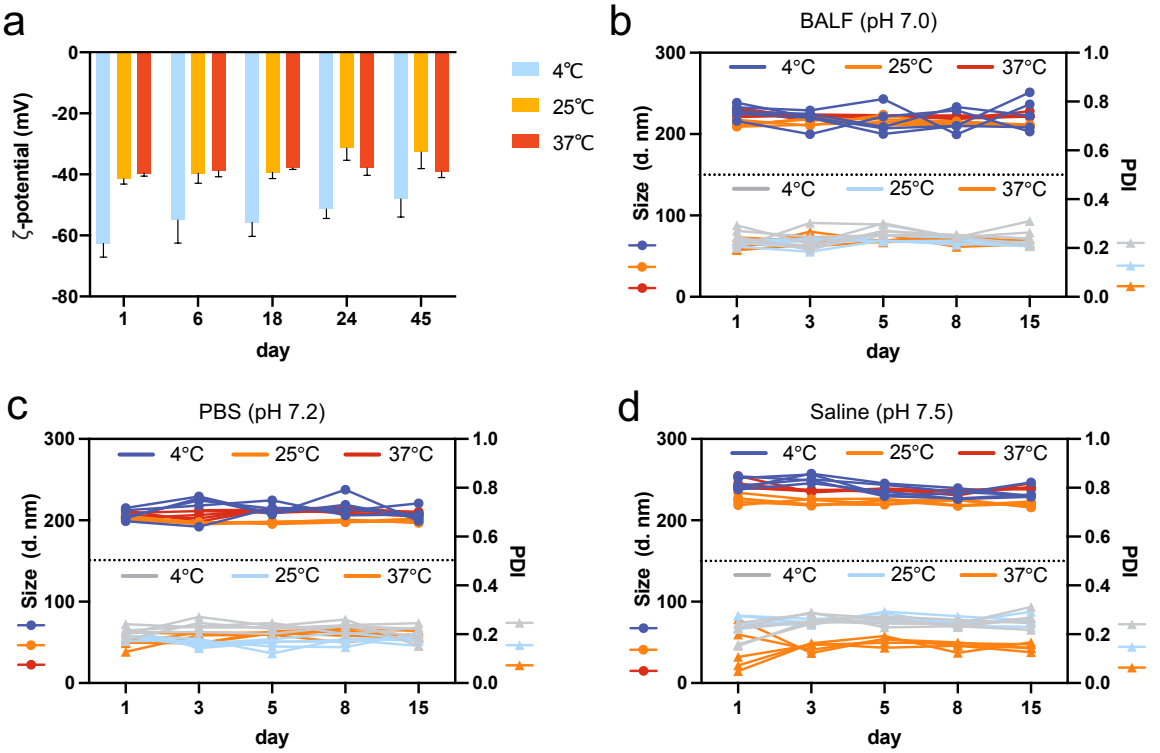

Supplementary Fig. 1. a. Measurement of diameter and zeta potential changes in PFCE-C25 NEs (n=5). b. The diameter size and PDI changes of PFCE-C25 NEs in mouse bronchoalveolar lavage fluid (BALF), PBS(c), or Saline (d) solutions are measured using DLS at different time intervals (1 d, 3 d, 5 d, 8 d, and 15 d).

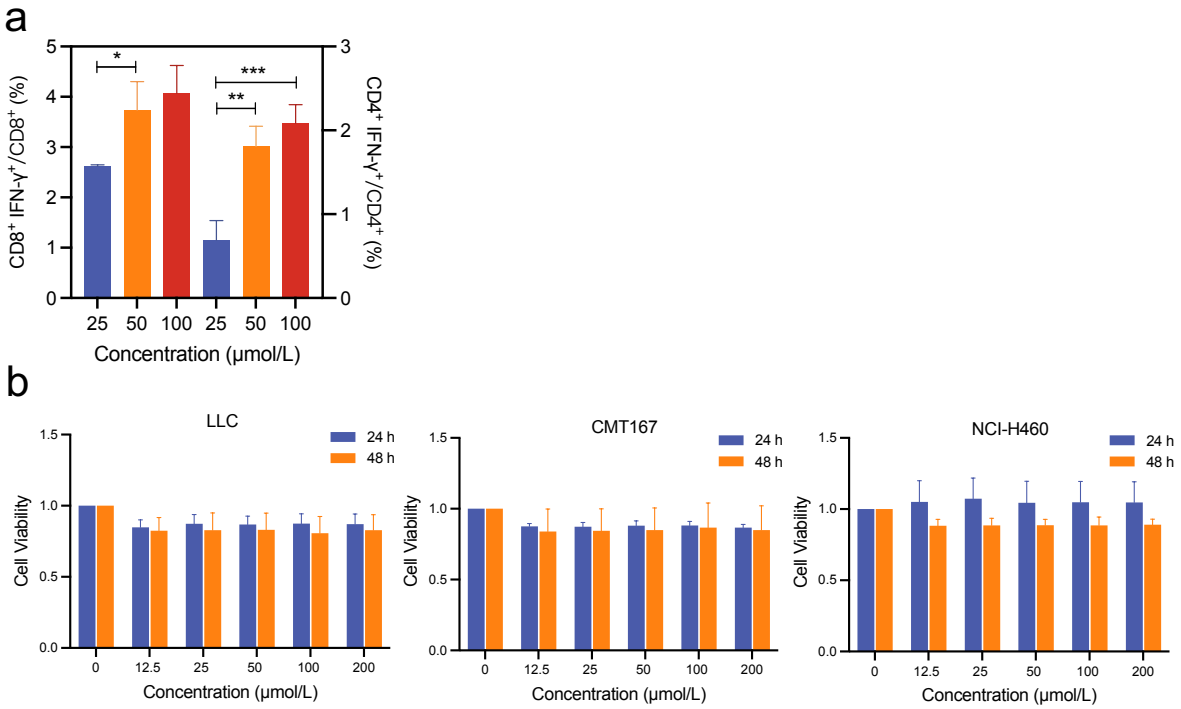

Supplementary Fig. 2. a. The ability of PFCE-C25 NEs to stimulate the secretion of IFN-γ by human PBMCs and increase the percentage of $CD8^+$ $IFN\text{-}\gamma^+$ T cells and $CD4^+$ $IFN\text{-}\gamma^+$ T cells (n=3). b. MTT analysis of the effect of PFCE-C25 NEs on the proliferation of LLC, CMT167 and NCI-H460 tumor cells in vitro (n=6). The data are presented as the mean ± SD.

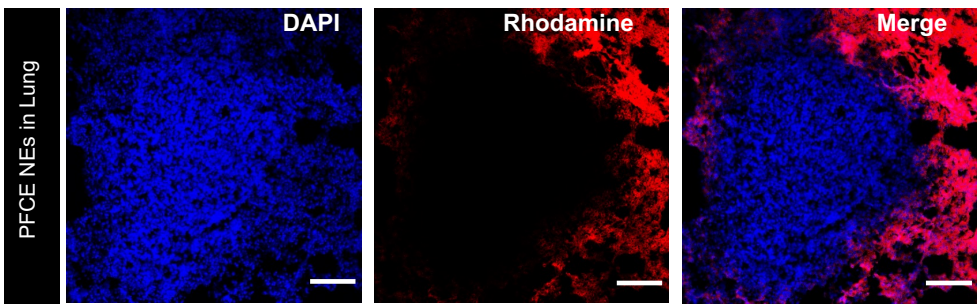

Supplementary Fig. 3. Distribution of PFCE NEs in LLC tumor-bearing lung tissue; scale bar: 100 μm.

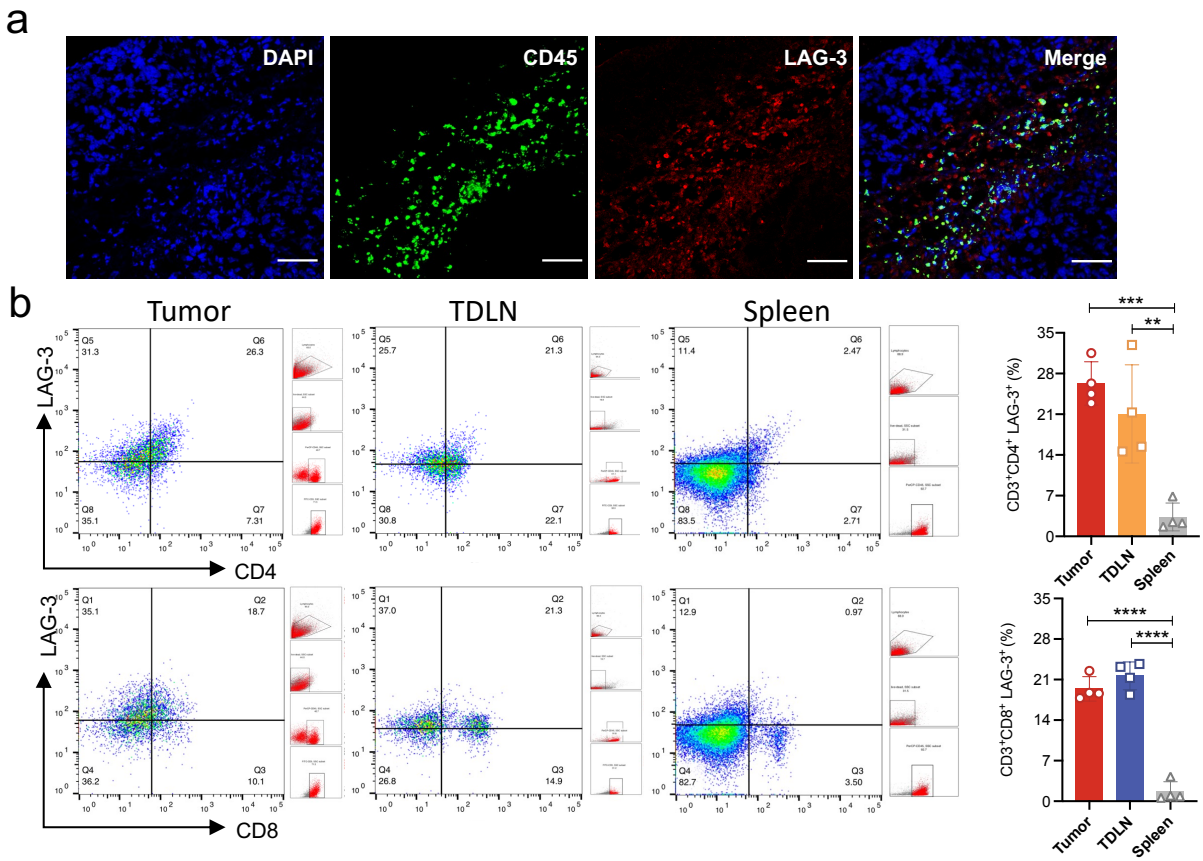

Supplementary Fig. 4. a. Immunofluorescence staining results showing LAG-3 expression in an LLC in situ lung cancer mouse model. b. Flow cytometry results showing LAG-3 expression in LLC in situ lung tumors. The data are presented as the mean ± SD, n=4.

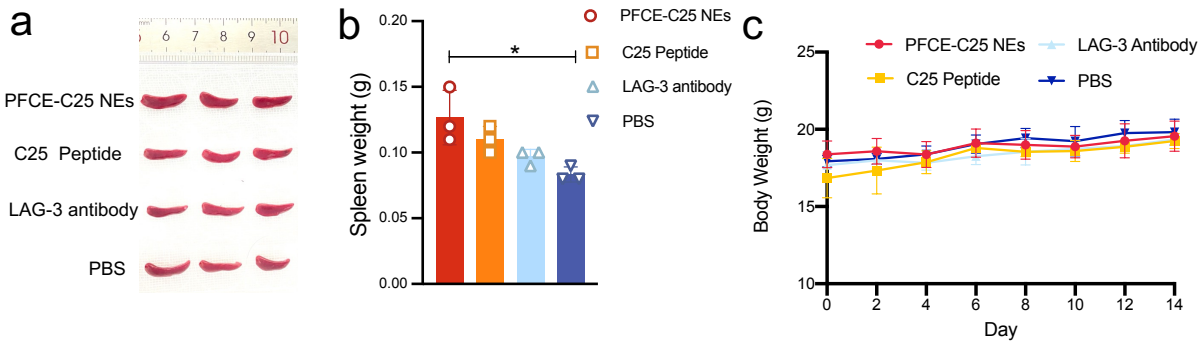

Supplementary Fig. 5. a. Spleen size and average spleen weight from each treatment group are shown (b), n=3. c. Changes in the body weight of LLC tumor-bearing mice in each treatment group, n ≥ 6. The data are presented as the mean ± SD.

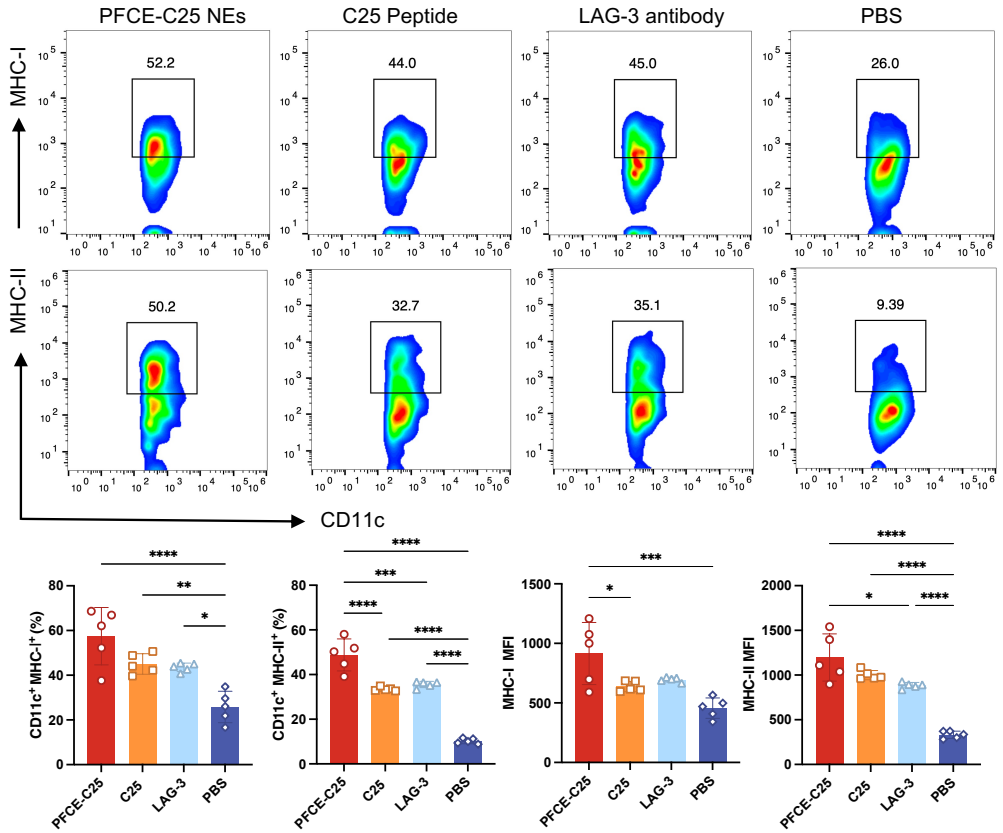

Supplementary Fig. 6. Expression of MHC I and MHC II in DCs within the tumor microenvironment of LLC in different treatment groups (n = 5). The data are presented as the mean ± SD.

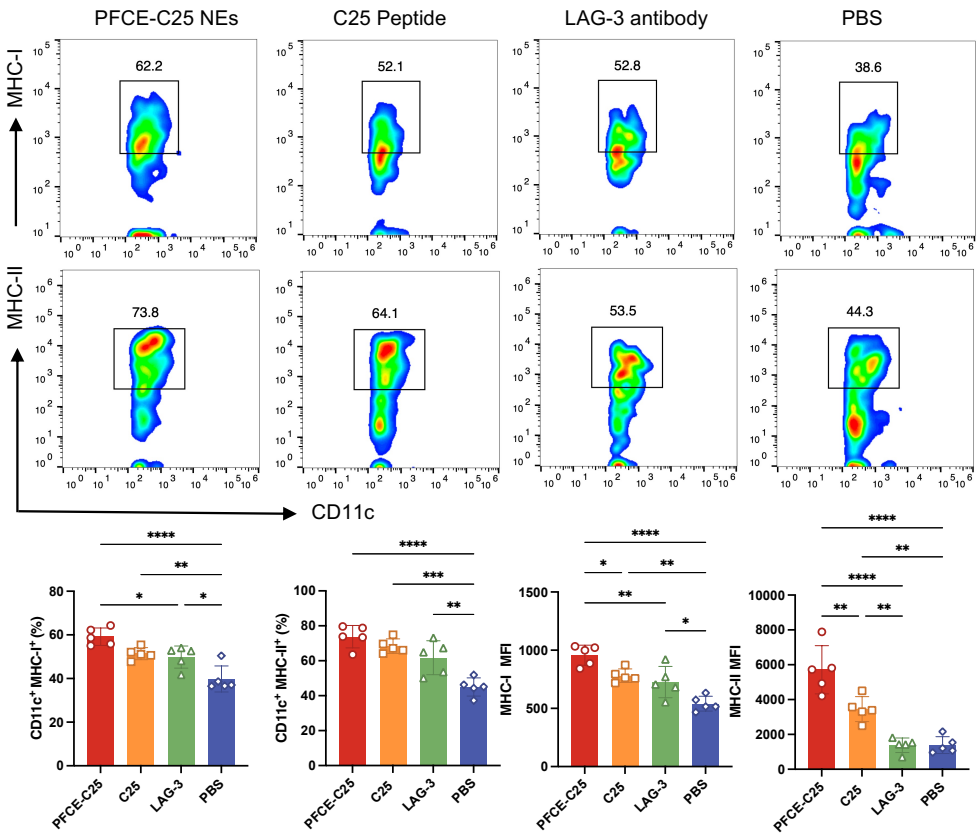

Supplementary Fig. 7. Expression of MHC I and MHC II in DCs within the LLC TDLN in different treatment groups (n = 5). The data are presented as the mean ± SD.

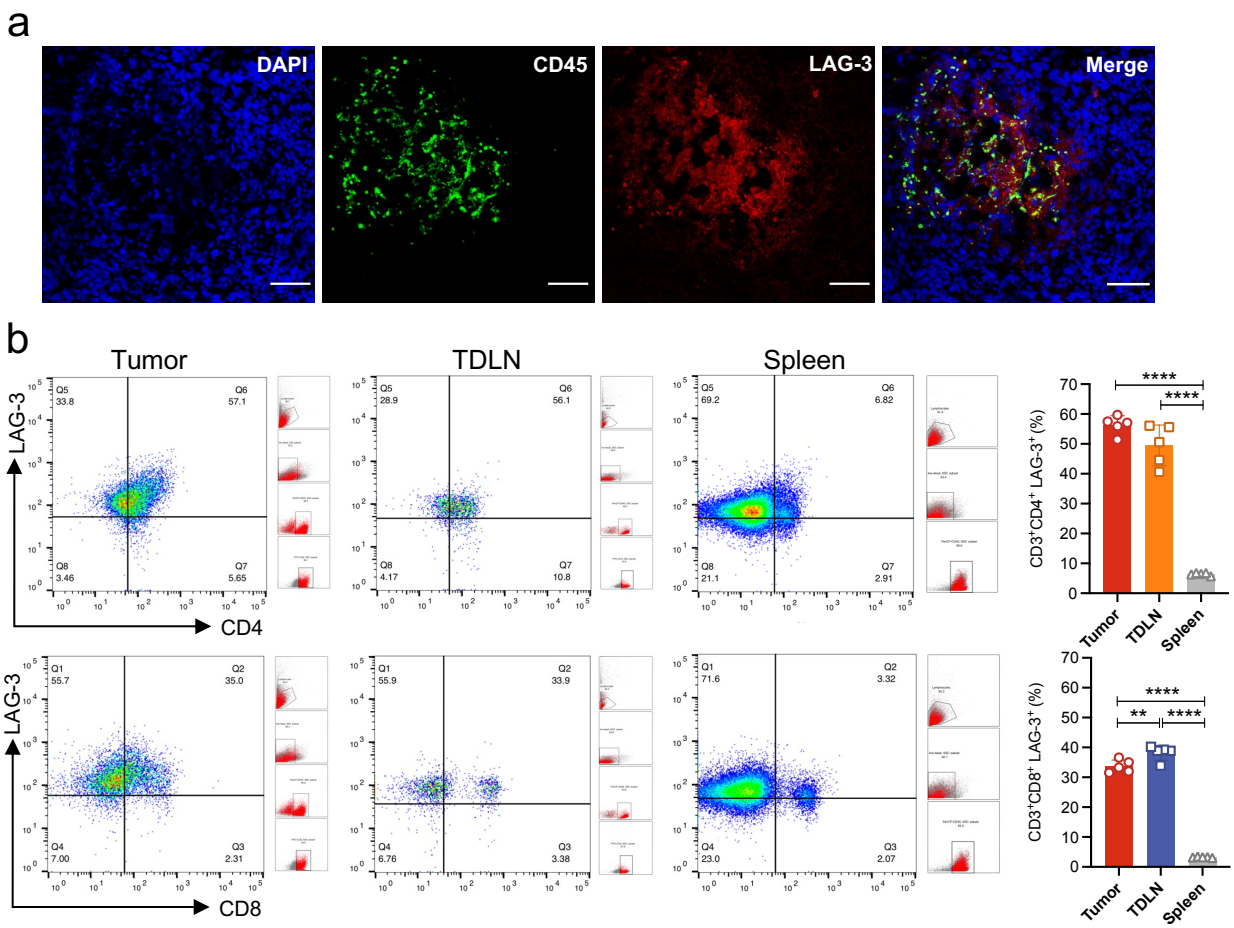

Supplementary Fig. 8. a. Immunofluorescence staining results showing LAG-3 expression in a CMT167 in situ lung cancer mouse model. b. Flow cytometry results showing LAG-3 expression in CMT167 in situ lung tumors. The data are presented as the mean ± SD, n=5.

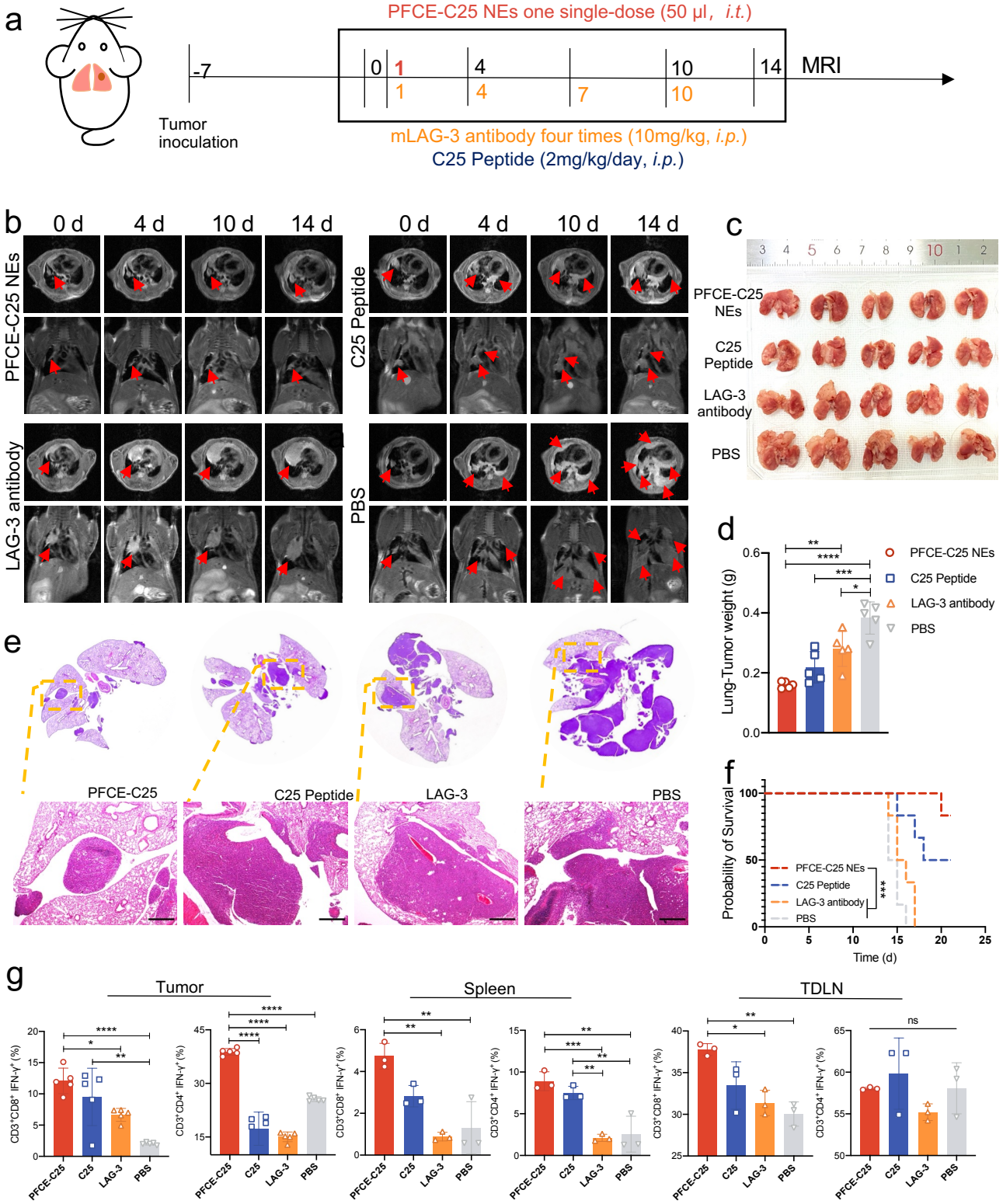

Supplementary Fig. 9. Therapeutic effect of PFCE-C25 NEs on the CMT167 in situ lung cancer model. a. Schematic diagram of the dosing and imaging regimen for each treatment group. b. MRI results for immunotherapy monitoring, red arrow points to tumor. c. Lung-solid tumor images of each research group. d. Weight statistics of lung-solid tumors of each group (n=5). e. Representative H&E staining results of the lungs of each treatment group, scale bar: 20 μm. f. Log-rank survival curve analysis. g. The ratio of $CD8^+$ $IFN\text{-}\gamma^+$ T cells and $CD4^+$ $IFN\text{-}\gamma^+$ T cells in the tumor (n=5), spleen (n=3) and TDLNs (n=3) of each treatment group. The data are presented as the mean ± SD.

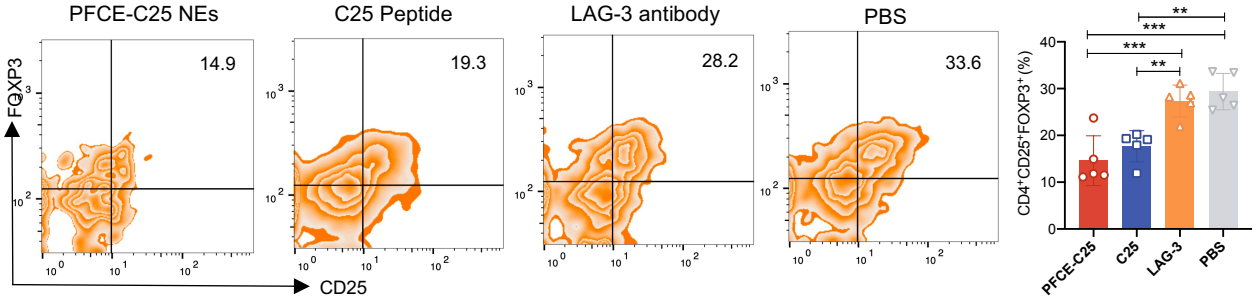

Supplementary Fig. 10. FOXP3$^+$ Treg infiltration in CMT167 in situ lung cancer tumors from each treatment group; n=5. The data are presented as the mean ± standard deviation (SD).

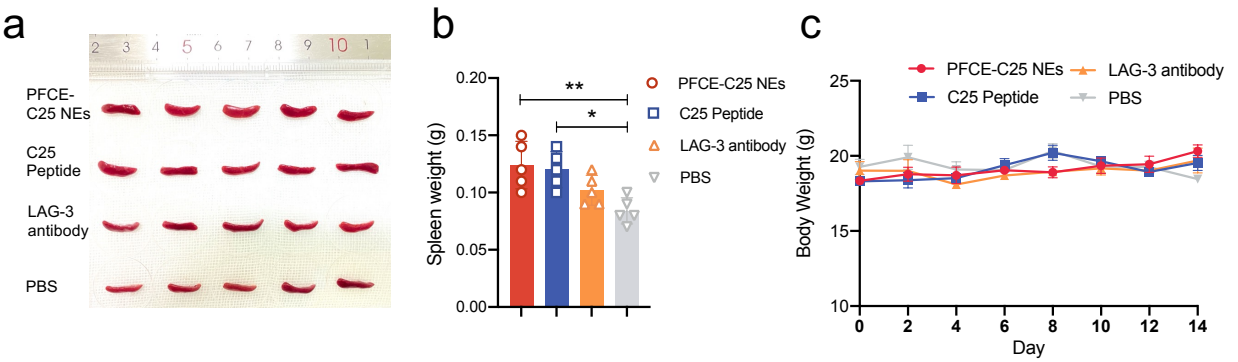

Supplementary Fig. 11. a. Spleen size and average spleen weight from each treatment group are shown (b). c. Changes in body weight of CMT167 lung tumor-bearing mice in each treatment group. The data are presented as the mean ± standard deviation (SD), n=5.

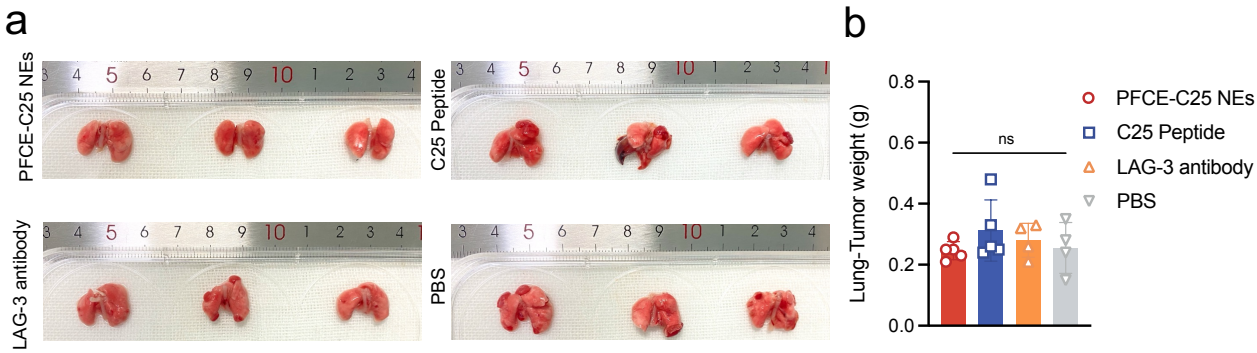

Supplementary Fig. 12. The PFCE-C25 NEs enhance local and distant tumor immune responses. a. Representative lung-solid tumor images from each research group, n = 4. b. Statistical analysis of the weights of the lung-solid tumors from each group. The data are presented as the mean ± SD, n ≥ 4.

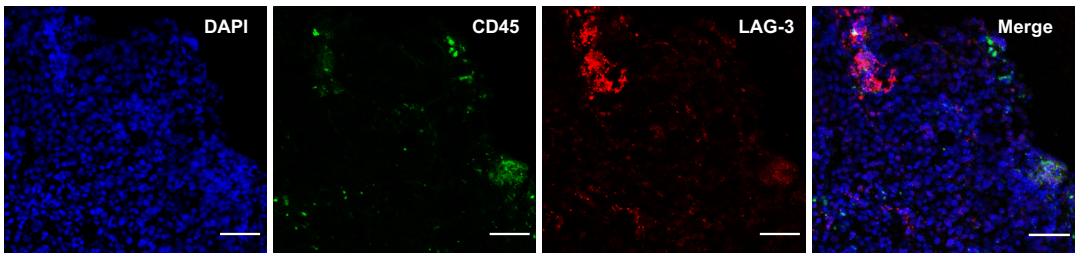

Supplementary Fig. 13. Immunofluorescence staining results showing LAG-3 expression in a humanized NCI-H460 in situ lung cancer mouse model.

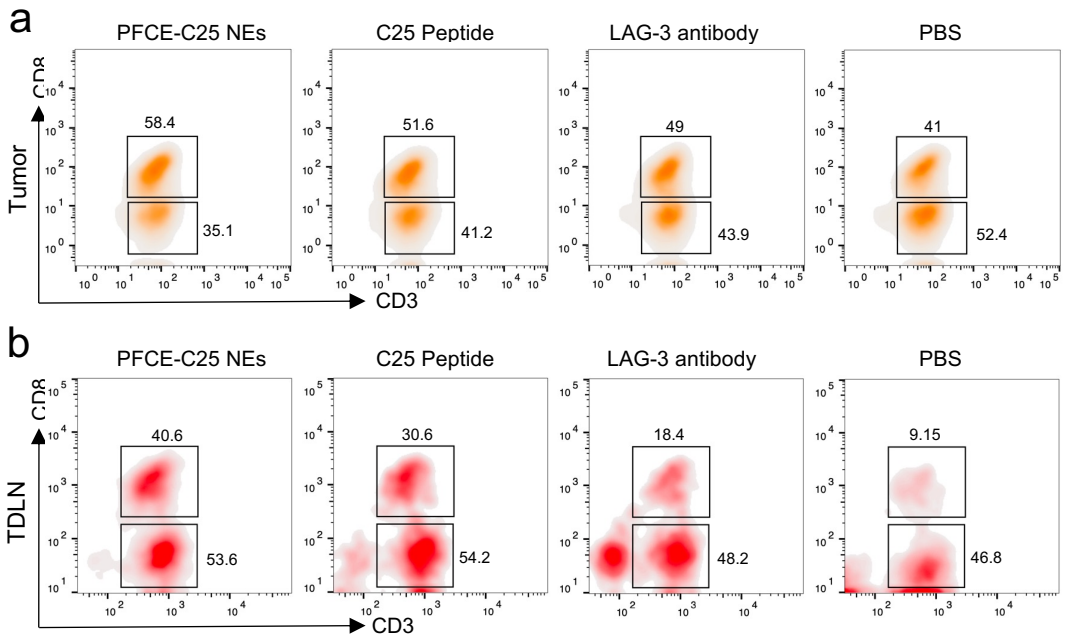

Supplementary Fig. 14. The immune function of PFCE-C25 NEs in a humanized in situ lung cancer model. a. $CD8^+$ T-cell and $CD4^+$ T-cell infiltration in tumors and TDLNs (b), n =5. The data are presented as the mean ± SD.

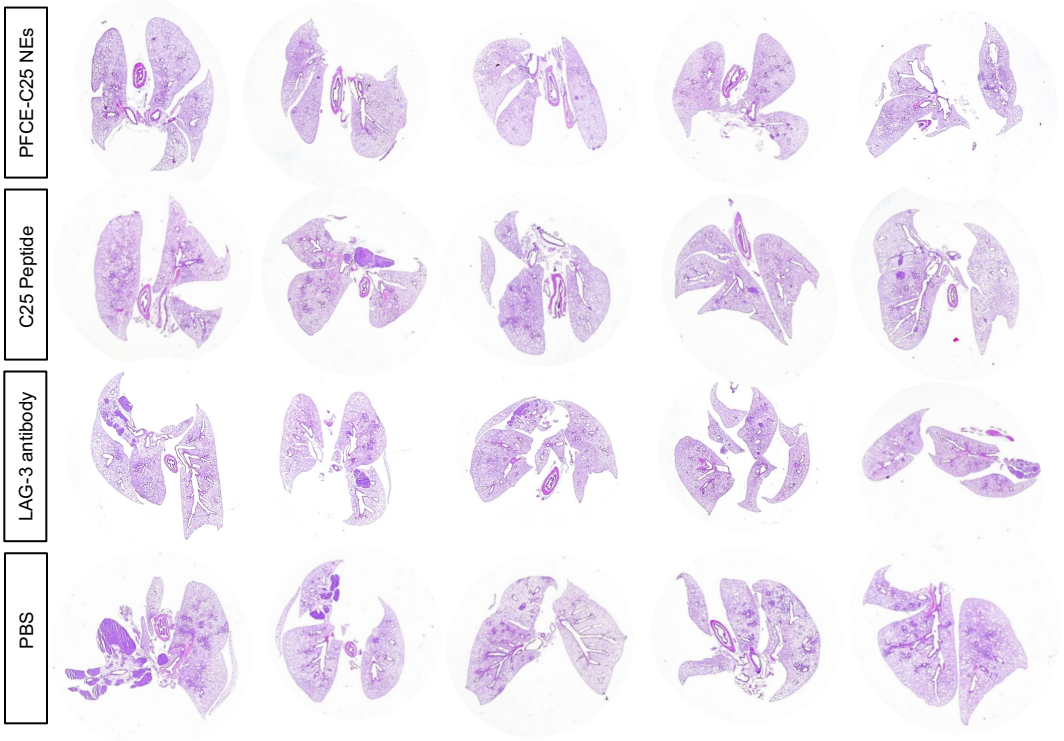

Supplementary Fig. 15. Representative H&E staining results of the lungs of the HIS NCI-H460 in situ lung cancer model mice in each treatment group; n=5.

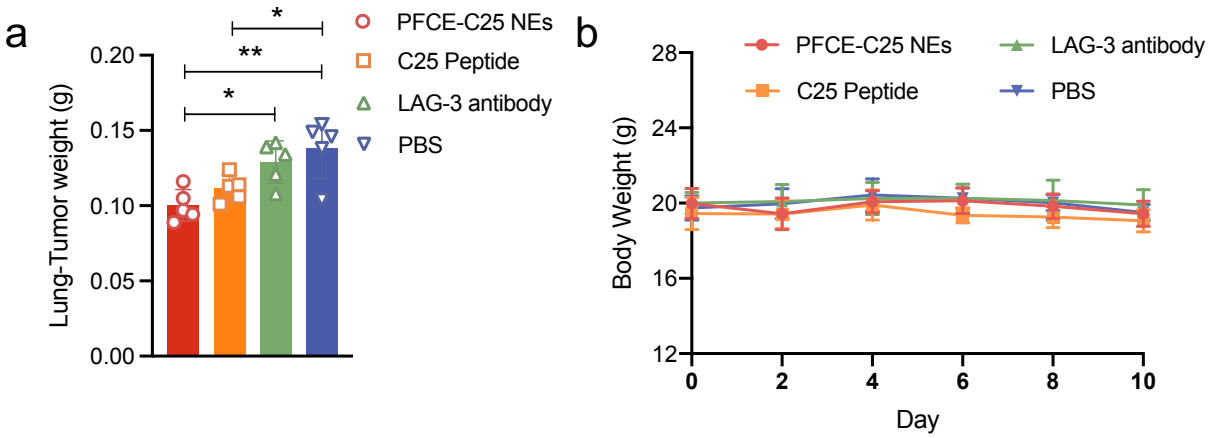

Supplementary Fig. 16. a. Lung-tumor weight and body weight changes in the humanized NCI-H460 in situ lung cancer model mice during treatment (b). The data are presented as the mean ± SD, n=5.

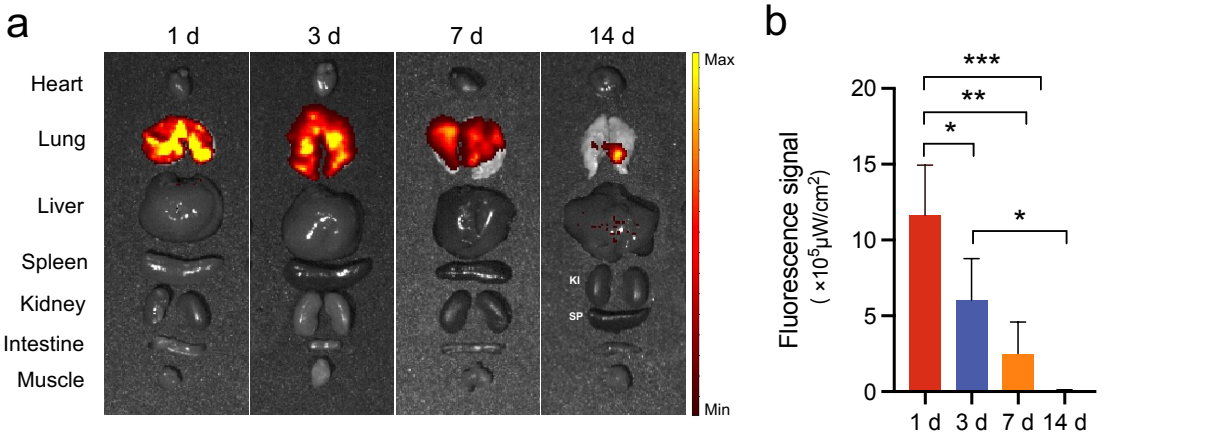

Supplementary Fig. 17. a. Representative IVIS imaging results of PFCE-C25 NEs after injection (50 μl) and the corresponding fluorescence signal analysis (b). The data are presented as the mean ± SD, n ≥ 3.

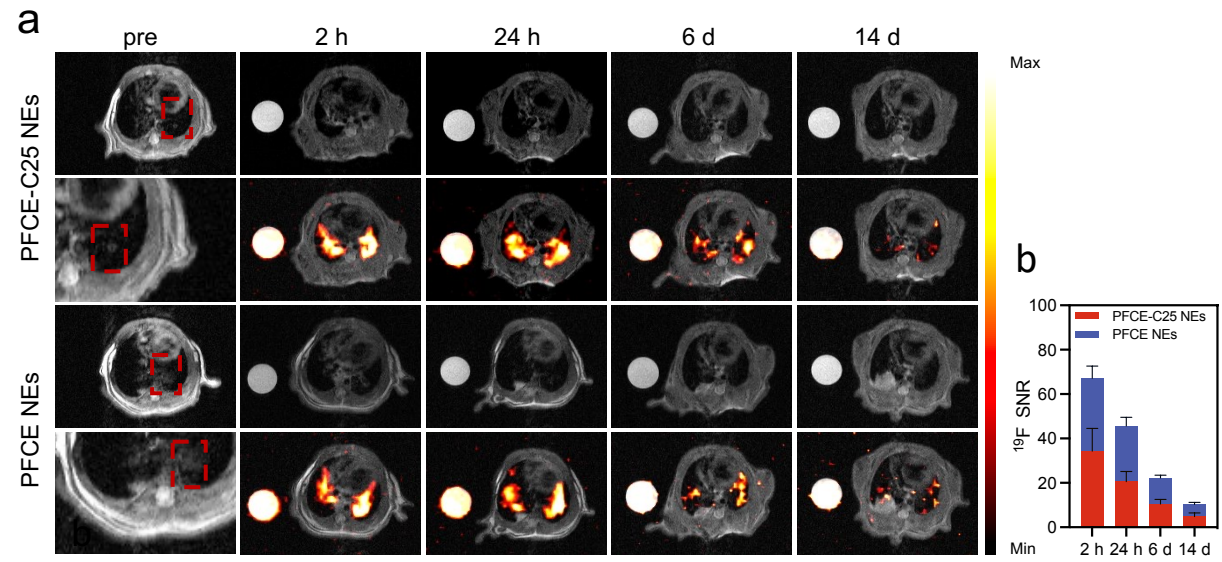

Supplementary Fig. 18. a. $^{1}H/^{19}F$ MR images after intratracheal administration of 50 μl of PFCE-C25 NEs or PFCE NEs at different time points and the corresponding ^{19}F SNR calculation (b).

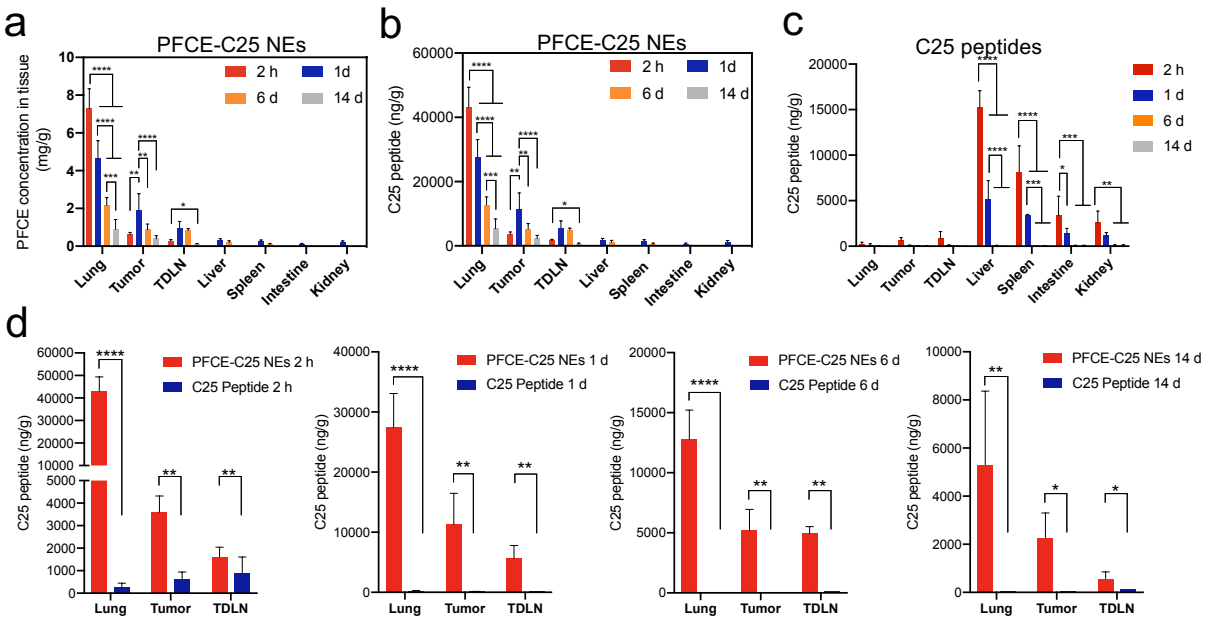

Supplementary Fig. 19. Quantitative analysis of the biological distribution of PFCE-C25 NEs (*i.t.*) and C25 peptides (*i.p.*). a. ^{19}F-NMR quantitative results of the PFCE concentration in major organs at different time points after injection and the corresponding statistical results for the C25 peptide content in main organs after PFCE-C25 NEs injection (b). c. Quantitative results of the C25 peptide content in major organs at different time points after injection determined by HPLC. d. Comparison of C25 peptide concentrations in the lungs, tumors and TDLNs of the PFCE-C25-NEs and C25 peptide injection groups at 2 h, 1 d, 6 d and 14 d. The data are presented as the mean ± SD, n=3.

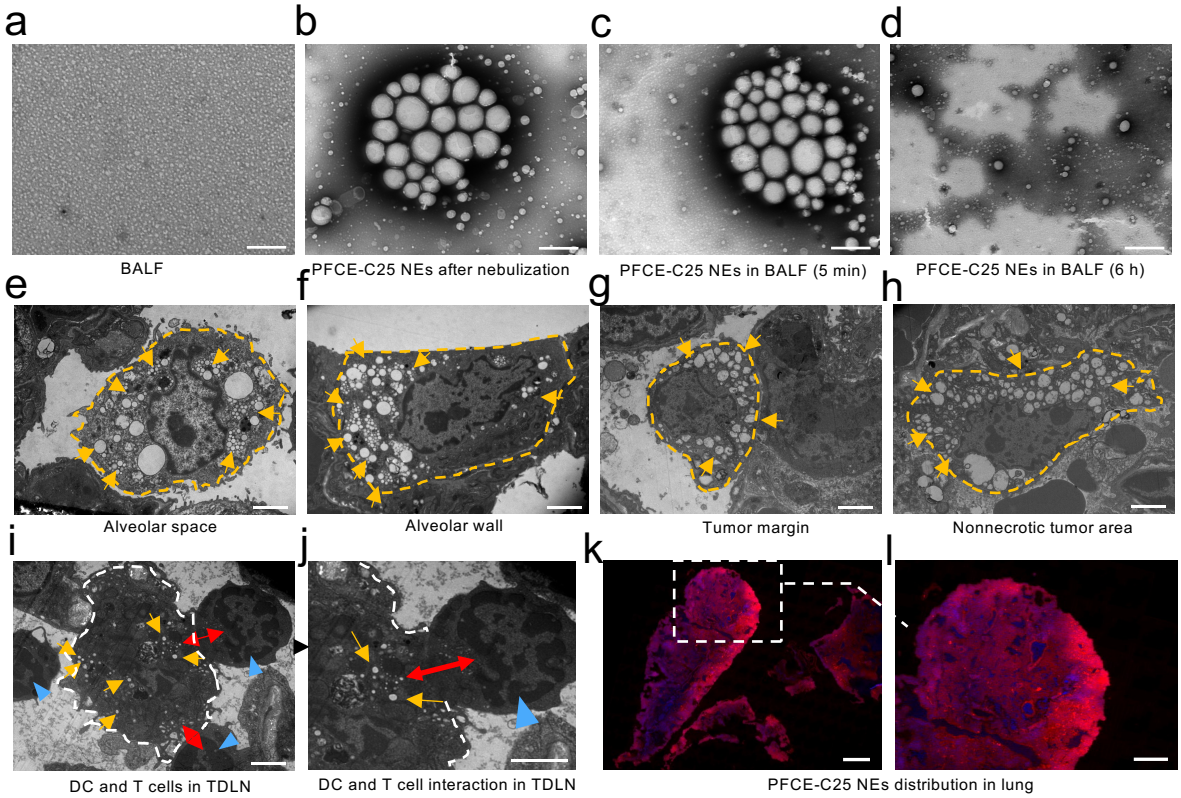

Supplementary Fig. 20. Distribution and administration by nebulization. a. TEM results of mouse bronchoalveolar lavage fluid (BALF). b TEM results of PFCE-C25 NEs after nebulization. c. The BALF from mice was analyzed using transmission electron microscopy (TEM) following the nebulization of PFCE-C25 NEs for a duration of 5 minutes or 6 hours (d), a-d scale bars: 400 nm; TEM images of the alveolar space(e), alveolar wall(f), tumor margin(g), nonnecrotic tumor area(h), DC and T cells in TDLN(i), as well as magnified TEM images of their interaction in TDLN(j) at 6 h after nebulization of PFCE-C25 NEs. e-j, scale bars: 2 μm. The yellow arrow indicates PFCE-C25 NEs, and the red arrow (two arrowheads) indicates the correlation between DCs and T cells.Yellow dotted lines, macrophages; White dotted lines, DCs; Blue triangle, T cell. k-l. Distribution of PFCE-C25 NEs in mouse lung tissue, scale bar: 1000 μm, 500 μm for magnification.

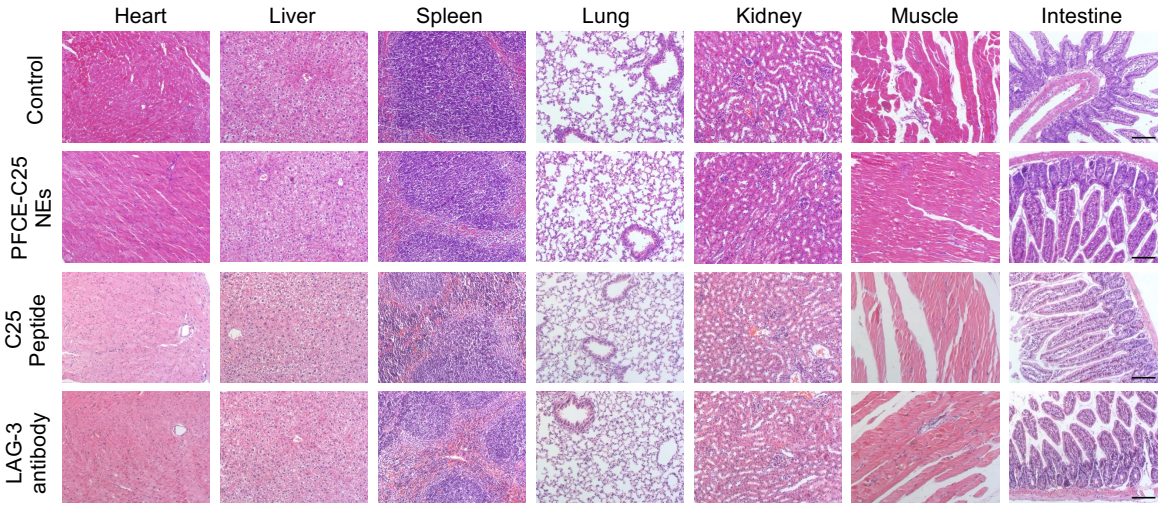

Supplementary Fig. 21. H&E staining of the main organs after injection of PFCE-C25 NEs, C25 peptides, or the LAG-3 antibody; scale bar, 100 μm.

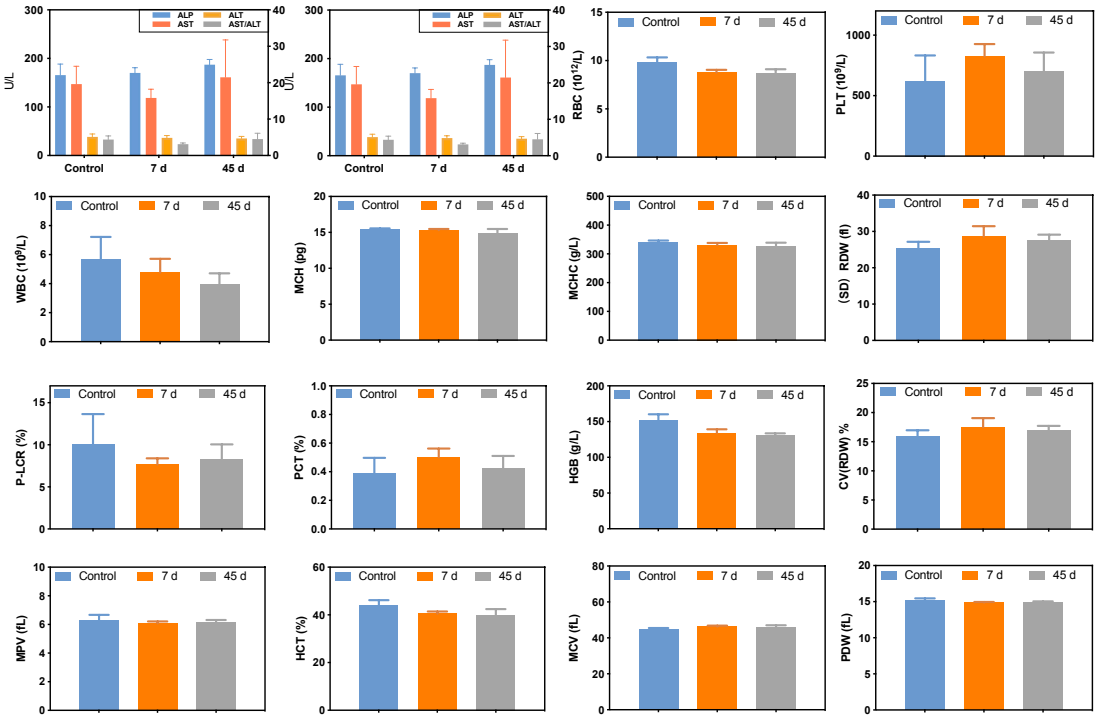

Supplementary Fig. 22. Corresponding hematological analysis of mice treated with saline or PFCE-C25 NEs. Red blood cell (RBC) count, platelet (PLT) count, white blood cell (WBC) count, mean corpuscular hemoglobin (MCH), mean corpuscular hemoglobin concentration (MCHC), red cell volume distribution width (RDW), platelet-larger cell ratio (P-LCR), procalcitonin (PCT), hemoglobin (HGB), coefficient of variation of RDW, CV (RDW), mean platelet volume (MPV), hematocrit (HCT), mean corpuscular volume (MCV) or platelet distribution width (PDW) were calculated. Blood samples were collected for hematological analysis on Day 7 and Day 45 after injection. The data are presented as the mean ± standard deviation (SD), $n \geq 3$.

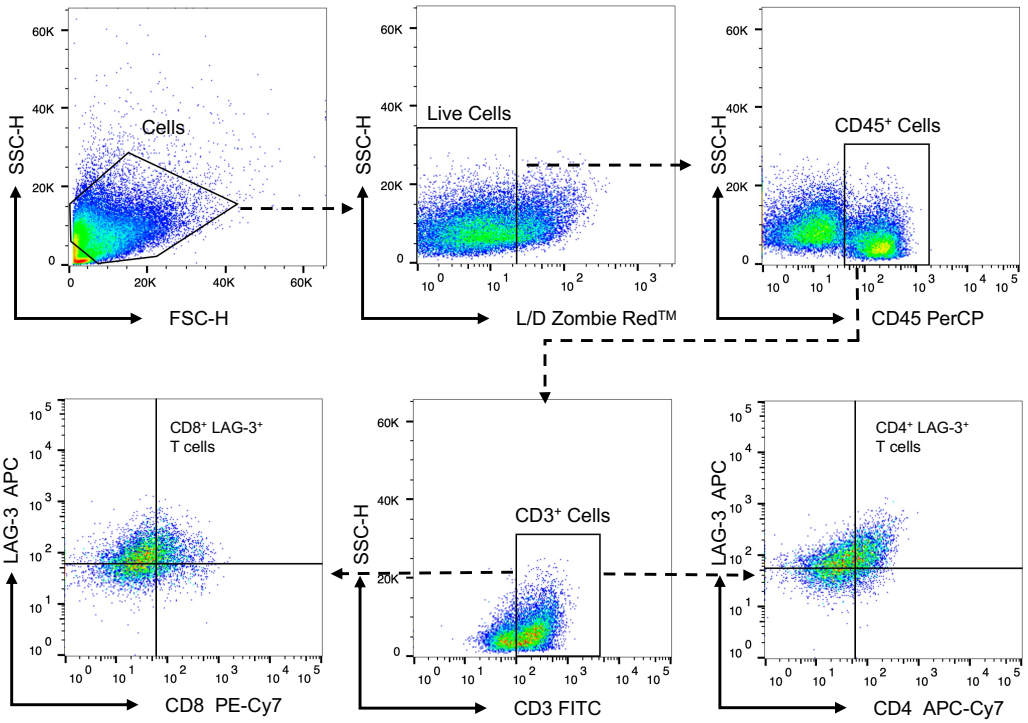

Supplementary Fig. 23. Exemplifying flow cytometry gating strategy for immune profiling of lung tumor microenvironment, spleen, and TDLN. Gating strategy corresponds to flow cytometric analysis in Fig. 10b, Supplementary Fig. 4, and Supplementary Fig. 8.

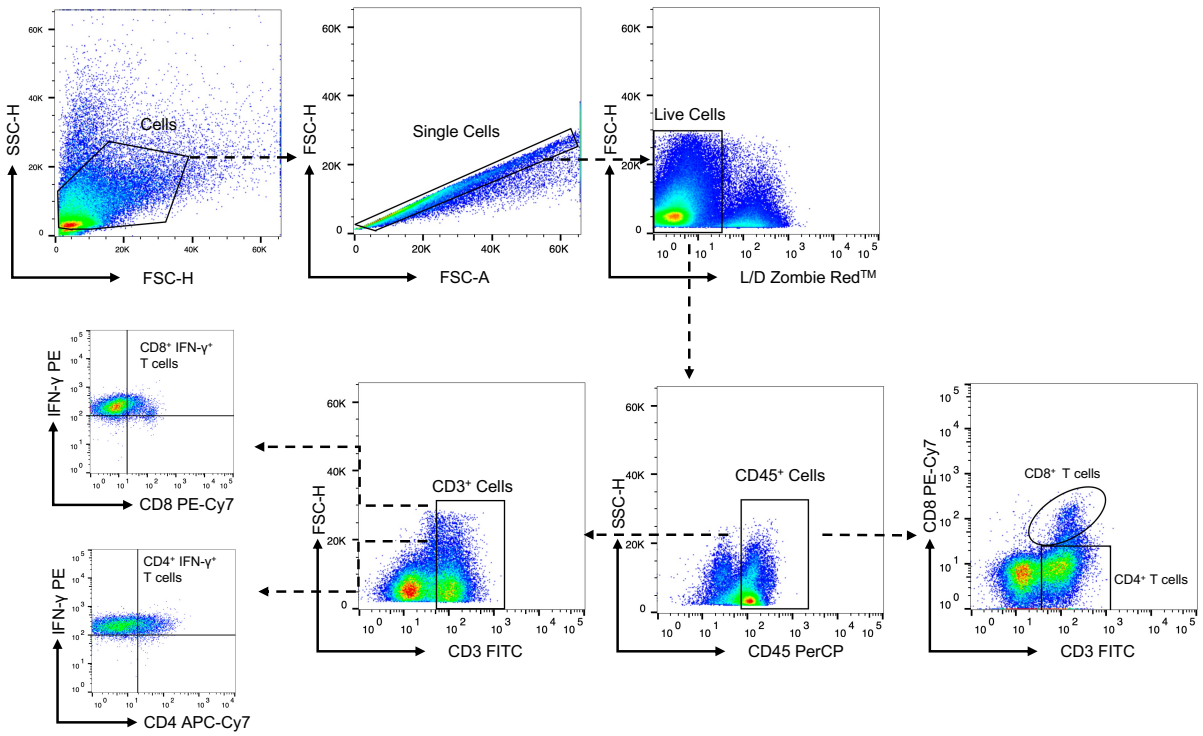

Supplementary Fig. 24. Exemplifying flow cytometry gating strategy for immune profiling of lung tumor microenvironment, spleen, and TDLN. Gating strategy corresponds to flow cytometric analysis in Fig. 3g, Fig. 6a,c, Fig. 10e,f, and Supplementary Fig. 9g.

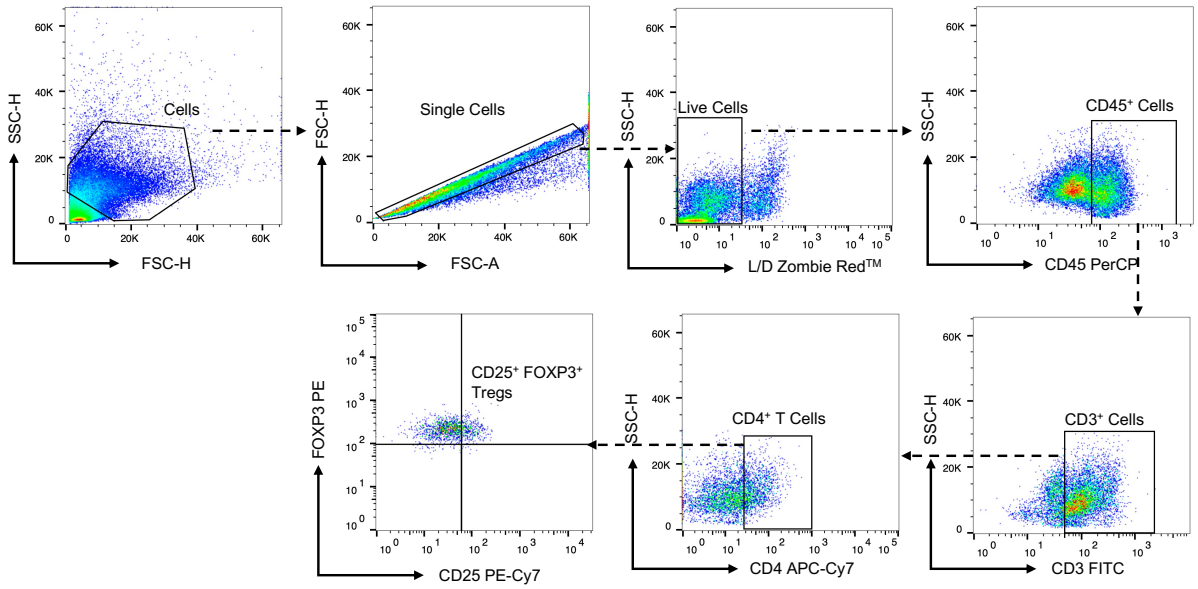

Supplementary Fig. 25. Exemplifying flow cytometry gating strategy for immune profiling of lung tumor microenvironment. Gating strategy corresponds to flow cytometric analysis in Fig. 6b, and Supplementary Fig. 10.

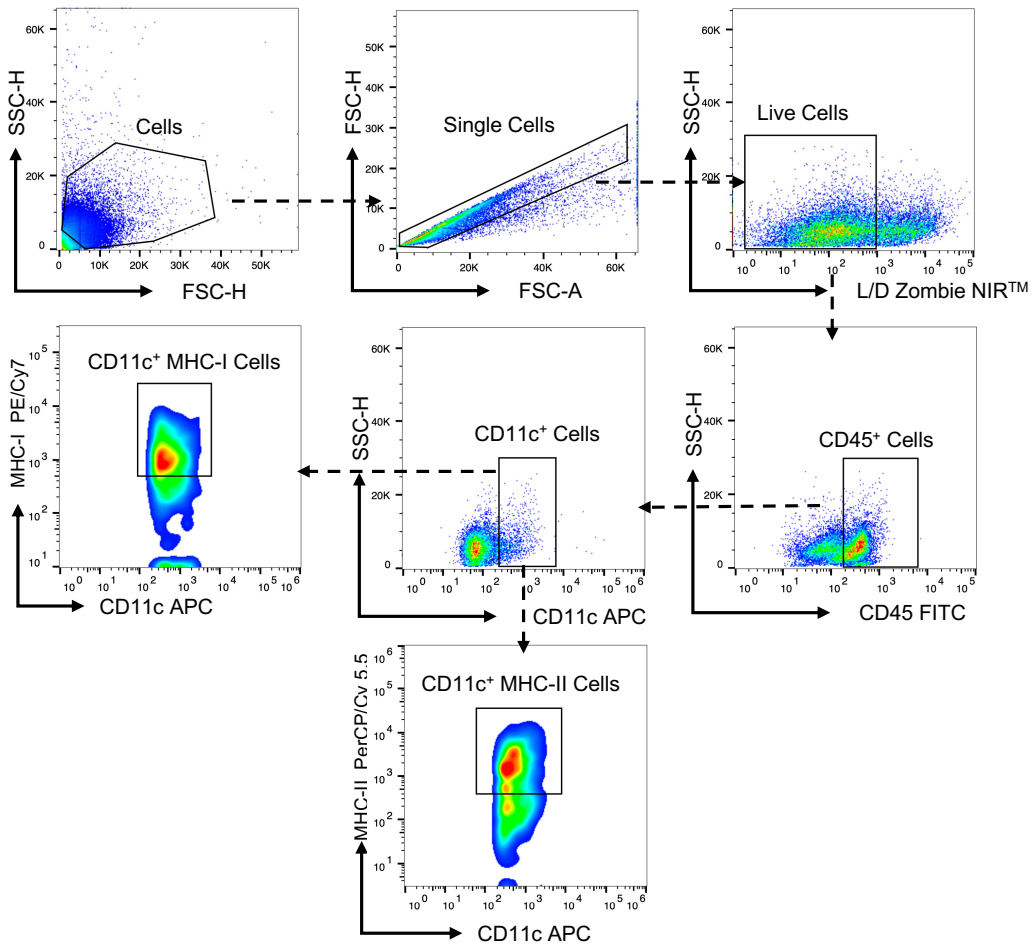

Supplementary Fig. 26. Exemplifying flow cytometry gating strategy for immune profiling of lung tumor microenvironment. Gating strategy corresponds to flow cytometric analysis in Supplementary Fig. 5 and Supplementary Fig. 6.

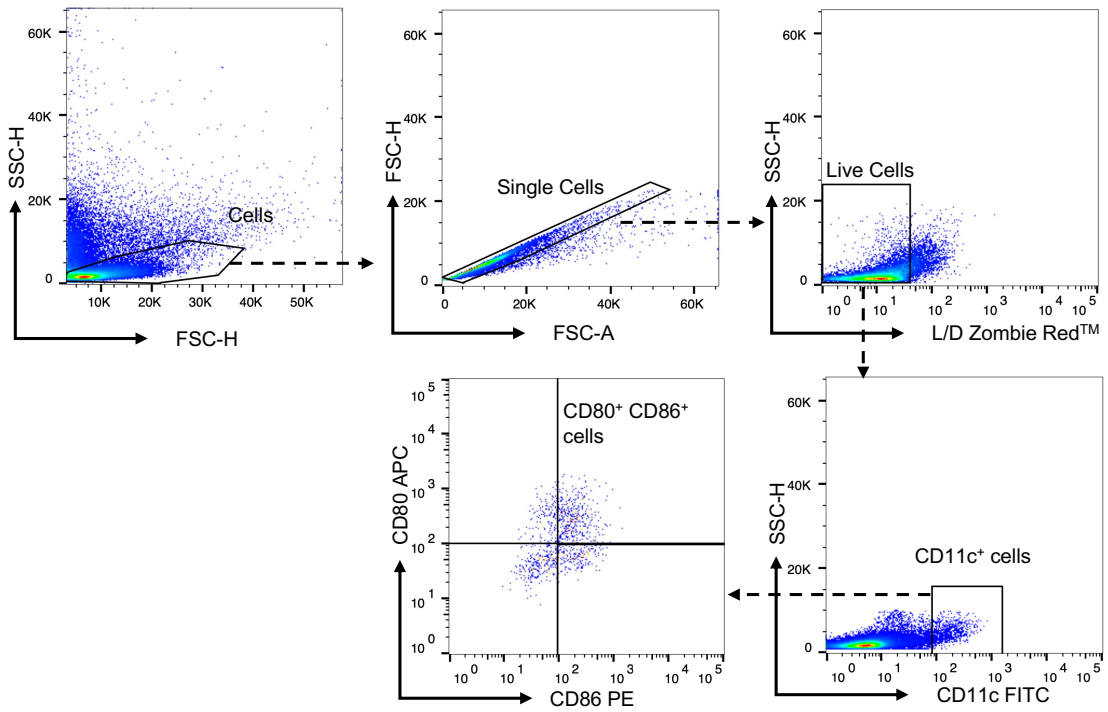

Supplementary Fig. 27. Exemplifying flow cytometry gating strategy for immune profiling of TDLN. Gating strategy corresponds to flow cytometric analysis in Fig. 4c.